

Strain engineering of oxide thin films for photocatalytic applications

Zhao Liu,^{1,2} Joel Shenoy,¹ Cesar Menéndez,¹ Judy N. Hart,¹ Charles C. Sorrell,¹ and Claudio Cazorla¹

¹*School of Materials Science and Engineering, UNSW Sydney, NSW 2052, Australia*

²*Sino-French Institute of Nuclear Engineering and Technology, Sun Yat-sen University, Zhuhai 519082, China*

Photocatalytic materials are pivotal for the implementation of disruptive clean energy applications such as conversion of H₂O and CO₂ into fuels and chemicals driven by solar energy. However, efficient and cost-effective materials able to catalyze the chemical reactions of interest when exposed to visible light are scarce due to the stringent electronic conditions that they must satisfy. Chemical and nanostructuring approaches are capable of improving the catalytic performance of known photoactive compounds however the complexity of the synthesized nanomaterials and sophistication of the employed methods make systematic design of photocatalysts difficult. Here, we show by means of first-principles simulation methods that application of biaxial stress, η , on semiconductor oxide thin films can modify their optoelectronic and catalytic properties in a significant and predictable manner. In particular, we show that upon moderate tensile strains CeO₂ and TiO₂ thin films become suitable materials for photocatalytic conversion of H₂O into H₂ and CO₂ into CH₄ under sunlight. The band gap shifts induced by η are reproduced qualitatively by a simple analytical model that depends only on structural and dielectric susceptibility changes. Thus, epitaxial strain represents a promising route for methodical screening and rational design of photocatalytic materials.

I. INTRODUCTION

The adverse effects of burning fossil fuels and the growing concentration of CO₂ in the atmosphere are motivating intense research efforts towards large-scale production of clean fuels and conversion of carbon dioxide into useful chemicals. In this context, generation of H₂ from water and reduction of CO₂ into methane (CH₄) and other valuable substances by using energy from sunlight represent two very promising sustainable approaches [1, 2].

Sunlight-induced dissociation of H–O and C–O bonds in water environment involves the use of photocatalytic materials that should fulfill quite stringent electronic requirements. For instance, the band gap (E_g) of photocatalytic materials must be below ~ 3 eV in order to absorb solar radiation within the visible spectral range. At the same time, a semiconductor able to catalyze the synthesis of H₂ in water or the reduction of CO₂ into CH₄ should possess a conduction-band edge higher in energy than the corresponding redox potential (-4.4 and -4.6 eV, respectively, relative to the vacuum level) and the valence-band edge lower than the H₂O oxidation potential (-5.6 eV) [2, 3]. Furthermore, active photocatalysis requires efficient separation of the photogenerated charge carriers (low exciton binding energy) and their rapid transportation to the reaction sites (long electron-hole recombination time) [4].

Cerium and titanium dioxide, CeO₂ and TiO₂, are two extensively investigated catalyst materials that present high structural stability, commercial availability, and low toxicity. Examples of applications in which CeO₂ and TiO₂ are exploited include fuel and solar cells, water purification, corrosion-resistant coatings, therapeutic agents, and gas sensors, to cite just a few [5–7]. Nevertheless, the band gap of both catalysts are larger than 3.0 eV, which severely restricts their absorbance of sunlight (to only $\approx 3\%$ of the solar irradiation that reaches

the earth’s surface [8]). Chemical and nanostructuring strategies have been employed successfully to reduce the band gaps of CeO₂ and TiO₂ and thus improve their photocatalytic activity under sunlight [9, 10]. Nevertheless, the usual complexity associated with the energy landscapes of nanomaterials and the required synthesis methods make it difficult to identify what key parameters improve photocatalytic efficiency irrespective of the material [4]. As a consequence, progress in “photocatalysis by design”, which is different from just ranking photocatalyst materials by their performance (“black box screening”), remains limited [11]. In addition to such design constraints, precious co-catalysts like Pt and Au typically are employed for improving photocatalytic performance, which is not suitable for practical applications [2, 8].

In this article, we show by means of first-principles simulations based on density functional theory that biaxial strain, η (which can be achieved in practice by growing thin films on substrates presenting a lattice parameter mismatch through, for example, pulsed laser deposition techniques [12, 13]), can be exploited to tune the optoelectronic and photocatalytic properties of some binary oxides in a substantial and controlled manner. Specifically, we predict that under feasible tensile strains of $\approx +2$ and $+3\%$ [14, 15] CeO₂ and TiO₂ become suitable materials for conversion of H₂O into H₂ and of CO₂ into CH₄ under sunlight. Such potential enhancements in photocatalytic activity result from sizeable band gap reductions ($\sim 10\%$) and correct positioning of the valence and conduction-band edges under η . Meanwhile, the effects of epitaxial strain on the band gap of ZnO, another well-known semiconductor photocatalyst [16], are found to be only marginal ($|\Delta E_g|/E_g \sim 1\%$). We present quantitative and physically intuitive arguments that explain the origins of such irregular η -driven effects on E_g in terms of dielectric susceptibility and metal-oxygen bond length changes.

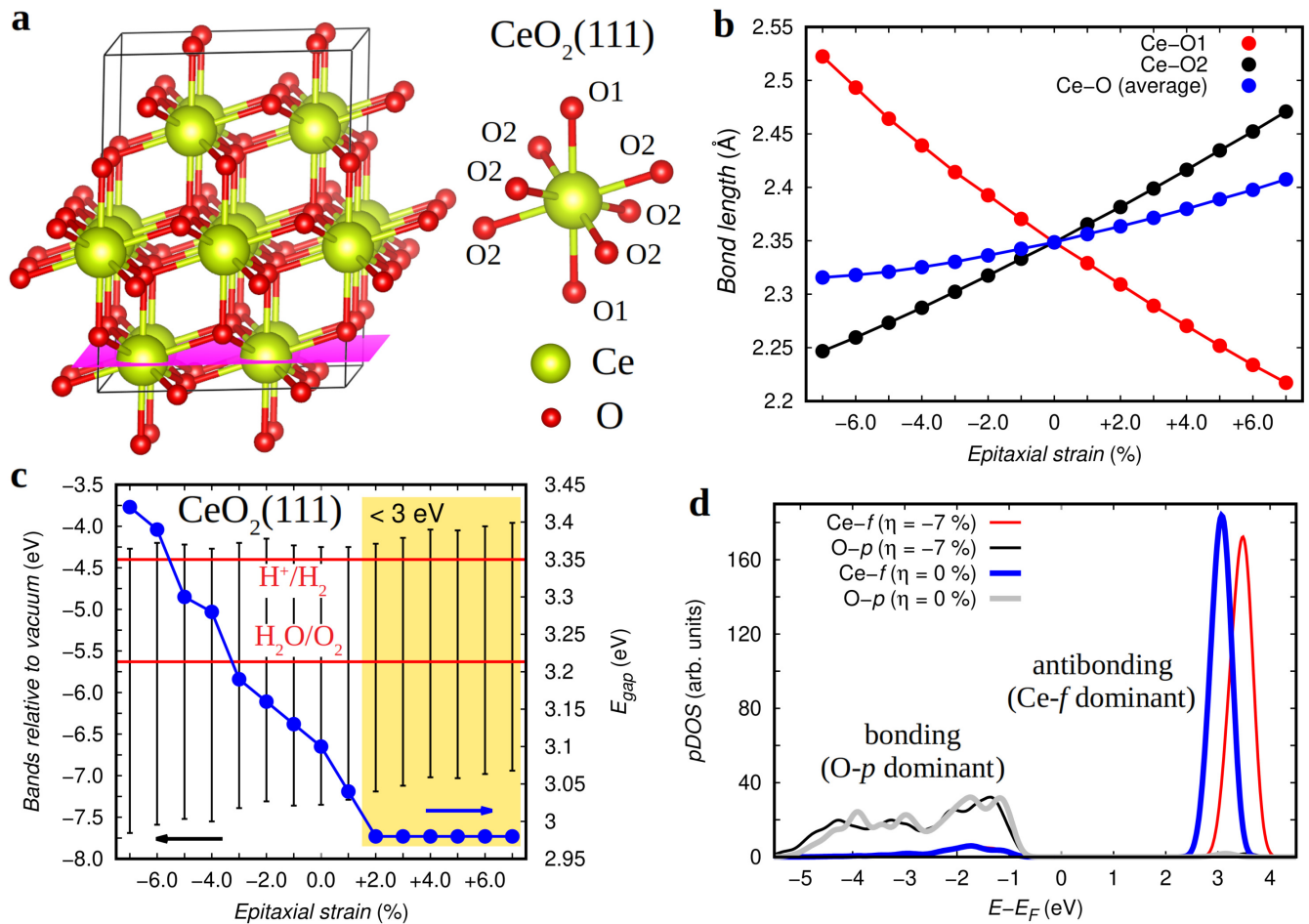


FIG. 1. Strain engineering of fluorite CeO_2 (111). **a** Atomic structure of the analyzed thin film system. The plane in which biaxial strain is applied is indicated in pink. The local oxygen environment of the Ce atoms is shown. **b** Variation of different Ce-O bond lengths as a function of biaxial strain. **c** Band gap and band alignment changes induced by epitaxial strain. The region in which the system band gap is lower than 3 eV is highlighted in yellow. The redox potentials of interest for water splitting are indicated with red horizontal lines. **d** Partial density of states calculated around the Fermi energy level at different η conditions.

It is worth noting that recent experimental and theoretical works have already proposed epitaxial strain as a means for tuning E_g in some oxide materials such as TiO_2 [17, 18], ZnO [16], SnO_2 [19], and CdO [20]. However, a clear and general understanding of how biaxial strain affects the photocatalytic performance of binary oxides is still missing. For instance, the relative E_g variations induced by tensile biaxial strain are negative in some materials (band gap decreases in TiO_2 and SnO_2 [17, 19]) whereas positive in others (band gap increases in ZnO [16]). Likewise, the E_g changes driven by compressive biaxial strain are positive in some materials (TiO_2 and SnO_2 [17, 19]) whereas negative or almost null in others (ZnO [16] and CdO [20]). These results indicate that the causes of η -induced band gap shifts cannot be traced down uniquely to simple structural changes [17, 19, 21] since those changes are quite monotonous under biaxial strain regardless of the material. Moreover, the influence of η on the band alignments of binary oxides has been ne-

glected in previous studies despite their potential impact on the photocatalytic activity. Hence, the present theoretical work identifies the key factors that drive η -induced band gap changes and fills the existing knowledge gaps. The results presented next show that strain engineering, either used on its own or as a complement to other existing approaches, can be a powerful tool for rational design and systematic improvement of photocatalytic materials.

II. FIRST-PRINCIPLES COMPUTATIONAL METHODS

First-principles calculations based on density functional theory (DFT) [22–24] are performed to simulate and analyze the influence of biaxial strain (η) on several representative binary oxide photocatalysts. We use the PBEsol functional [25] as is implemented in the VASP software package [26]. A “Hubbard- U ” scheme [27] with

$U = 3$ eV is employed for a better treatment of the localized Ce $4f$, Ti $3d$, and Zn $3d$ electronic orbitals. We use the “projector augmented wave” method to represent the ionic cores [28] by considering the following electrons as valence: Ce $4f$, $5d$, $6s$, and $4d$; Gd $4f$, $5d$, and $6s$; Ti $3d$, $4s$, $3p$, and $3s$; Zn $3d$ and $4s$; and O $2s$ and $2p$. Wave functions are represented in a plane-wave basis truncated at 650 eV. For integrations within the Brillouin zone we employ Monkhorst-Pack \mathbf{k} -point grids [29] with a density equivalent to that of $16 \times 16 \times 16$ in the fluorite CeO_2 unit cell. Strained-bulk geometry relaxations are performed with a conjugate-gradient algorithm that allows for volume variations while imposing the structural constraints defining thin films ($|a| = |b|$ and $\alpha = 90^\circ$) [30–33]. Periodic boundary conditions are applied along the three directions defined by the lattice vectors, so that possible surface effects are completely avoided in the simulations. The relaxations are halted when the forces acting on the atoms fall below $0.01 \text{ eV} \cdot \text{\AA}^{-1}$. By using these technical parameters we obtain zero-temperature energies that are converged to within 0.5 meV per formula unit. Biaxial strain conditions are simulated at $\Delta\eta = 1\%$ intervals. In order to estimate accurate band gaps and band alignments, we employ the hybrid HSE06 exchange-correlation functional [34] to perform single-point calculations on the equilibrium geometries determined at the PBEsol+ U level [3]. The generation of non-stoichiometric and Gd-doped fluorite CeO_2 thin films are explained in the Supplementary Methods along with some details of their energy and structural properties.

To calculate accurate band alignments we follow the work done by Moses and co-workers on binary semiconductors [35]. Briefly, both bulk and slab calculations are performed from which the alignment of the electrostatic potential within the semiconductor material can be obtained relative to the vacuum level. From the slab calculations, the difference between the average electrostatic potential within the semiconductor material and in vacuum is obtained. From the bulk calculations, the band structure shifts relative to the average electrostatic potential are determined. These calculations are performed at each η point and involve the estimation of macroscopic and planar average potentials (Supplementary Methods). The planar potential is computed by averaging potential values within a well defined plane (for instance, perpendicular to the surface of the slab), and the macroscopic potential is obtained by taking averages of the planar potential over distances of one unit cell along the chosen direction [36, 37]. The slab systems should be thick enough to ensure that the electron density in the center of the slab is practically equal to that in the bulk material. We have found that 1.2–1.8 nm thick oxide slabs accompanied by similarly large portions of vacuum provide sufficiently well converged results for the electrostatic potentials. Further technical details of our band alignment calculations are provided in the Supplementary Methods.

III. RESULTS AND DISCUSSION

The changes induced by biaxial strain, η , on the structural, electronic, and photocatalytic properties of CeO_2 , TiO_2 , and ZnO as calculated with first-principles methods based on density functional theory (DFT, Sec. II and Supplementary Methods) are presented first. Both compressive ($\eta < 0$) and tensile ($\eta > 0$) biaxial strains ranging from zero up to a maximum absolute value of 7% have been considered in the simulations. These values are comparable in magnitude to the η 's achieved experimentally in the same materials [14–16]. At the end of this section, we introduce a simple analytical model that depends only on structural and dielectric susceptibility changes and reproduces qualitatively, and helps in understanding, the general band gap trends induced by η .

A. Fluorite CeO_2 (111)

At room temperature, bulk ceria (CeO_2) presents a cubic phase known as fluorite (space group $Fm\bar{3}m$) in which the Ce ions form a face centered cubic sublattice and the oxygens a simple cubic. Ceria thin films commonly exhibit three high-symmetry orientations $\{111\}$, $\{011\}$, and $\{001\}$. In this section, we consider the $\{111\}$ case; results for the $\{001\}$ geometry will be presented in the next section.

In the fluorite structure each Ce ion is surrounded by eight equidistant oxygens. Upon application of (111) biaxial strain, some crystal symmetries are broken (space group changes to $R\bar{3}m$) and two characteristic metal-oxygen bond lengths emerge, Ce–O1 and Ce–O2, which are six- and two-fold degenerate, respectively (Fig.1a). The Ce–O1 bonds are oriented perpendicular to the (111) plane, in which the strain is applied, and thus under compressive (tensile) biaxial strain they are stretched (reduced). Conversely, the Ce–O2 bonds, which are mostly contained within the (111) plane, are shortened (stretched) under compressive (tensile) biaxial strain (Fig.1b). Due to the higher degeneracy of the Ce–O2 bonds, the average metal-oxygen neighbouring length decreases under compressive biaxial strain and increases under tensile η (Fig.1b). For instance, at the maximum simulated compressive (tensile) biaxial strain the average Ce–O distance is reduced (elongated) by 1.4 (2.5)% of the unstrained value.

The sizable structural changes induced by η suggest the possibility of finding similarly large variations in the band gap (E_g) of (111)-oriented CeO_2 thin films [17, 19]. In fact, as shown in Fig.1c, this turns out to be the case. Specifically, E_g increases practically linearly under compressive biaxial strain, reaching a maximum value of 3.4 eV at $\eta = -7\%$. According to our DFT calculations the band gap of unstrained CeO_2 is 3.1 eV, which compares very well with the experimental value of 3.2 eV [38], hence a maximum relative E_g increase of 10% is achieved. Under tensile biaxial strain, E_g also varies significantly

although not in a regular manner. The band gap first decreases to below 3.0 eV at $\eta \approx +2\%$ but beyond that strain point its value remains practically constant (Fig.1c). As a result, a maximum η -driven E_g reduction of 4% is obtained. It is worth noting that the largest E_g variation is achieved under compressive η whereas the largest average Ce–O length change is achieved under tensile strain. This observation suggests that, at least for (111)–oriented CeO₂ thin films, the band gap shifts induced by η cannot be explained exclusively in terms of the accompanying structural changes.

Figure 1c also shows the band alignments of (111)–oriented CeO₂ thin films, that is, the energy level of the valence-band (VB) and conduction-band (CB) edges as a function of η . In the absence of any strain, our calculations predict a VB edge located at -7.3 eV and CB at -4.2 eV with respect to the vacuum level, which are in fairly good agreement with the available experimental data ($E_{\text{VB}}^{\text{expt}} = -6.9$ eV and $E_{\text{CB}}^{\text{expt}} = -4.1$ eV [39]). For photocatalytic water-splitting purposes, the electronic band structure of unstrained CeO₂ (111) presents two important limitations. First, the corresponding E_g is too large for absorption of visible light, and second, the position of the VB (CB) edge is too far below (too close to) the water oxidation potential of -5.6 eV (the proton reduction potential of -4.4 eV) [2, 3]. Interestingly, biaxial strain can be used to partly overcome both of those limitations. Under tensile strain, the energy of the VB edge increases steadily and becomes equal to -6.9 eV at $\eta = +7\%$, 0.4 eV closer to the water oxidation potential than for unstrained CeO₂. At the same strain, the CB edge reaches a maximum value of -4.0 eV and the band gap becomes smaller than 3 eV. Thus, under $\eta > 0$ sunlight can be absorbed more efficiently and the VB and CB edges are situated more appropriately for water splitting (that is, 1.3 eV below and 0.4 eV above the corresponding redox potentials). Meanwhile, under compressive strain the energy of the VB edge decreases steadily and the CB level remains more or less constant. As a consequence, the band gap of CeO₂ (111) increases almost linearly with increasing strain magnitude in the $\eta < 0$ region. We note that the band gap of unstrained bulk ceria is indirect and remains so in the investigated η interval (Supplementary Figure 1).

The influence of biaxial strain on the VB and CB edges of CeO₂ (111) (and thus on the band gap, defined as $E_g \equiv E_{\text{CB}} - E_{\text{VB}}$) can be understood in terms of the concomitant electronic and structural changes. In bulk ceria, the top of the VB is mostly composed of oxygen $2p$ orbitals that form a bonding state with Ce $4f$ orbitals, while the bottom of the CB is mostly composed of cerium $4f$ orbitals that form an antibonding state with O $2p$ orbitals (Fig.1d). Compressive (tensile) strain reduces (increases) the average Ce–O bond length, which energetically favors (frustrates) the bonding state. Consequently, the energy of the VB edge decreases under $\eta < 0$ and increases under $\eta > 0$. On the other hand, the bottom of the CB is found to be quite insensitive to compressive

strains (Fig.1c). When the anion-cation bond lengths are reduced, the kinetic energy associated with the antibonding state typically increases (since it is proportional to k^2 , where k represents the reciprocal lattice vector in the extended Brillouin zone) [40]; that increase in kinetic energy would bring the CB higher in energy. However, the p – f level repulsion appears to diminish slightly under compressive strain owing to the increased delocalization of the Ce $4f$ orbitals (see density of states peaks above the Fermi energy level in Fig.1d, where the Ce $4f$ states extend over a wider energy range for $\eta < 0$). These two effects tend to oppose each other thus leaving the CB edge unaffected by compressive strain. Under tensile strain, the energy of the antibonding state eventually rises due to a significant increase in the localization of the Ce $4f$ orbitals (Supplementary Figure 2) which enhances the p – f level repulsion and overcomes the accompanying decrease in kinetic energy.

B. Fluorite CeO₂ (001)

Upon application of (001) biaxial strain, the degeneracy of the eight equidistant oxygens surrounding each Ce ion (characteristic distance Ce–O1 in Fig. 2a) is not lifted, but the symmetry of the crystal changes from cubic to tetragonal (space group $I4/mmm$) due to contraction or elongation of the out-of-plane c axis relative to the two in-plane lattice vectors $a = b$ (Fig.2b). The changes driven by (001) strain on E_g are noticeably different from those found in the (111) case (Figs.2c and 1c). In particular, the band gap now is hardly affected by compressive strain but is significantly reduced under tensile strain. For instance, at $\eta = +7\%$ the band gap is 2.2 eV, $\approx 30\%$ lower than the value obtained at equilibrium conditions; at $\eta \approx +3\%$, E_g is already smaller than 3.0 eV. Plots of the electronic energy bands indicate that the band gap remains indirect regardless of η (Supplementary Figure 3), as for the CeO₂ (111) thin films.

The influence of η on the band edges of (001)–oriented CeO₂ thin films can also be rationalized in terms of the accompanying structural and electronic changes. In this case, we have not explicitly calculated the band alignments however, in analogy to the (111) case, we assume that the energy of the VB edge decreases under $\eta < 0$ (increases under $\eta > 0$) due to enhancement (frustration) of the p – f bonding interactions induced by shortening (elongation) of the Ce–O1 bonds. Based on this assumption and there being no effect of compressive strain on the band gap, it is expected that the energy of the CB edge decreases under compressive strain due to increased delocalization of the unoccupied Ce $4f$ orbitals (Supplementary Figure 4), which weakens the p – f antibonding interactions and counteracts the concurrent increase in kinetic energy [40]. Hence, both the VB and CB edges decrease under $\eta < 0$ producing no net change in the band gap. Under tensile strain, however, it can be inferred from the decrease in the band gap that the bottom of

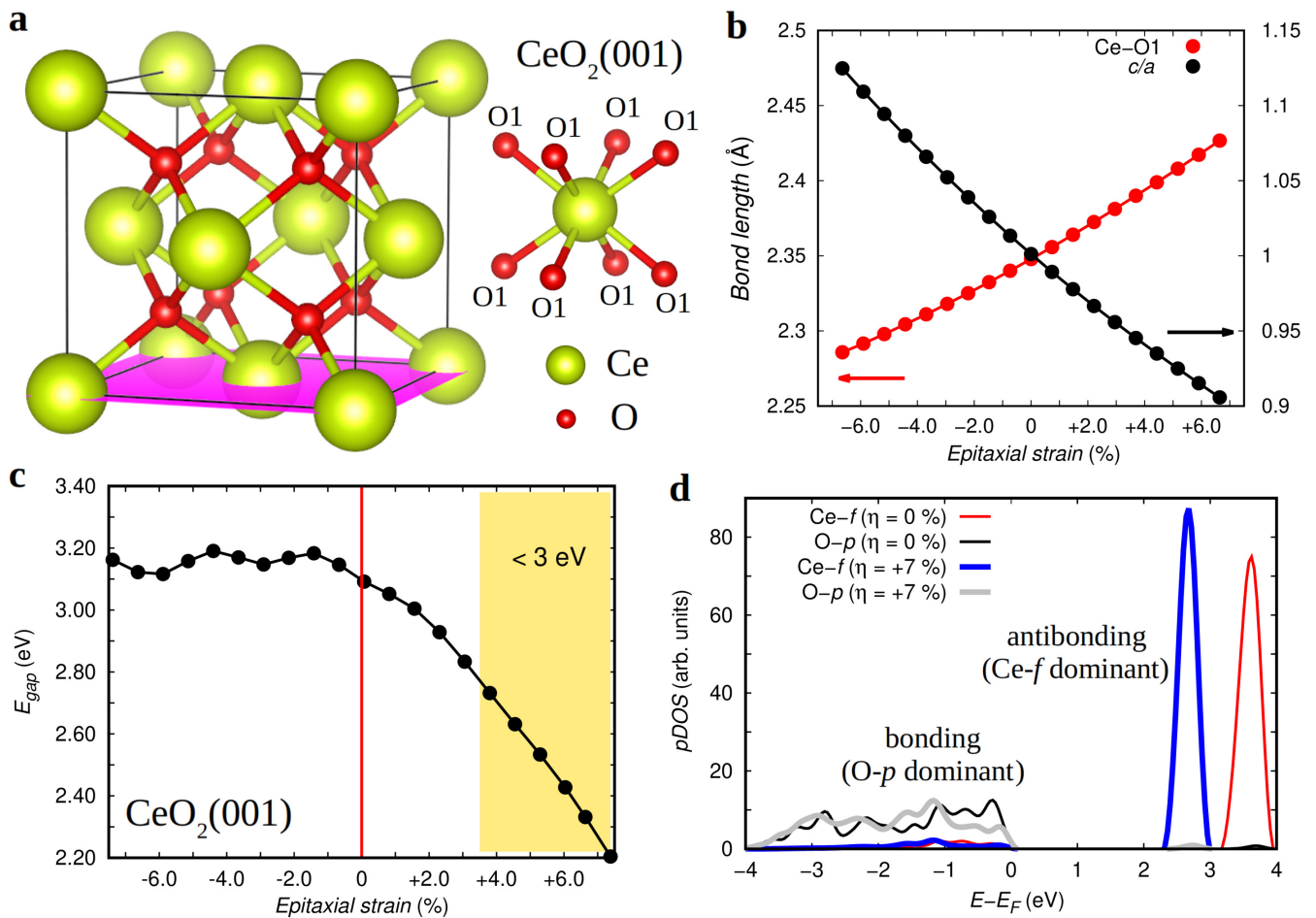


FIG. 2. Strain engineering of fluorite CeO₂ (001). **a** Atomic structure of the analyzed thin film system. The plane in which biaxial strain is applied is indicated in pink. The local oxygen environment of the Ce atoms is shown. **b** Variation of different structural parameters as a function of biaxial strain. **c** Band gap changes induced by epitaxial strain. The region in which the system band gap is lower than 3 eV is highlighted in yellow. **d** Partial density of states calculated around the Fermi energy level at different η conditions.

the conduction band remains more or less constant with respect to the vacuum level, possibly due to a compensation effect between the increased localization of the Ce 4*f* orbitals (see density of states peaks above the Fermi energy level in Fig.2d, where the Ce 4*f* states extends over a narrower energy range for $\eta > 0$), which tends to bring the CB higher in energy, and the reduction in kinetic energy, which tends to lower it.

It has been demonstrated thus far that biaxial strain can have a significant impact on the optoelectronic properties of stoichiometric CeO₂. It is reasonable to ask then whether similar control of functionality can be achieved in non-stoichiometric and metal-doped ceria thin films with $\eta \neq 0$, which can be prepared through advanced synthesis techniques [41, 42]. The results shown in Fig.3 indicate that this is indeed the case. Our simulations of non-stoichiometric ceria, CeO_{2- δ} , considering an arbitrary but representative δ of 0.125 [41] (Sec. II and Supplementary Methods), show that both positive and negative η 's can be used to reduce substantially E_g (by $\sim 10\%$

of the value obtained at zero strain, which is 2.1 eV), with tensile strain being particularly effective (Fig.3a). Band gaps of 1.7 and 1.4 eV are obtained respectively at the highest compressive and tensile strain values considered in this study. These sizable E_g reductions result from the combined action of oxygen vacancies, which are known to reduce the neighbouring Ce⁴⁺ ions and lower the CB edge due to the appearance of new unoccupied 4*f* states (Fig.3b) [41], and biaxial strain.

Likewise, in Ce_{1-2*x*}Gd_{2*x*}O_{2-*x*} (001) thin films with an arbitrary but representative composition of $x = 0.03$ [42], our DFT simulations (Sec. II and Supplementary Methods) indicate that tensile strain is also capable of reducing E_g considerably (Fig.3c). For instance, at $\eta = +7\%$ the band gap of Gd-doped ceria is 1.7 eV, which is approximately 30% smaller than the value estimated at zero strain (2.5 eV). In Gd-doped ceria, the presence of Gd³⁺ ions prevents the reduction of Ce⁴⁺ ions surrounding the oxygen vacancies (in contrast to what occurs in CeO_{2- δ}). As a consequence, the relative E_g variation induced by η

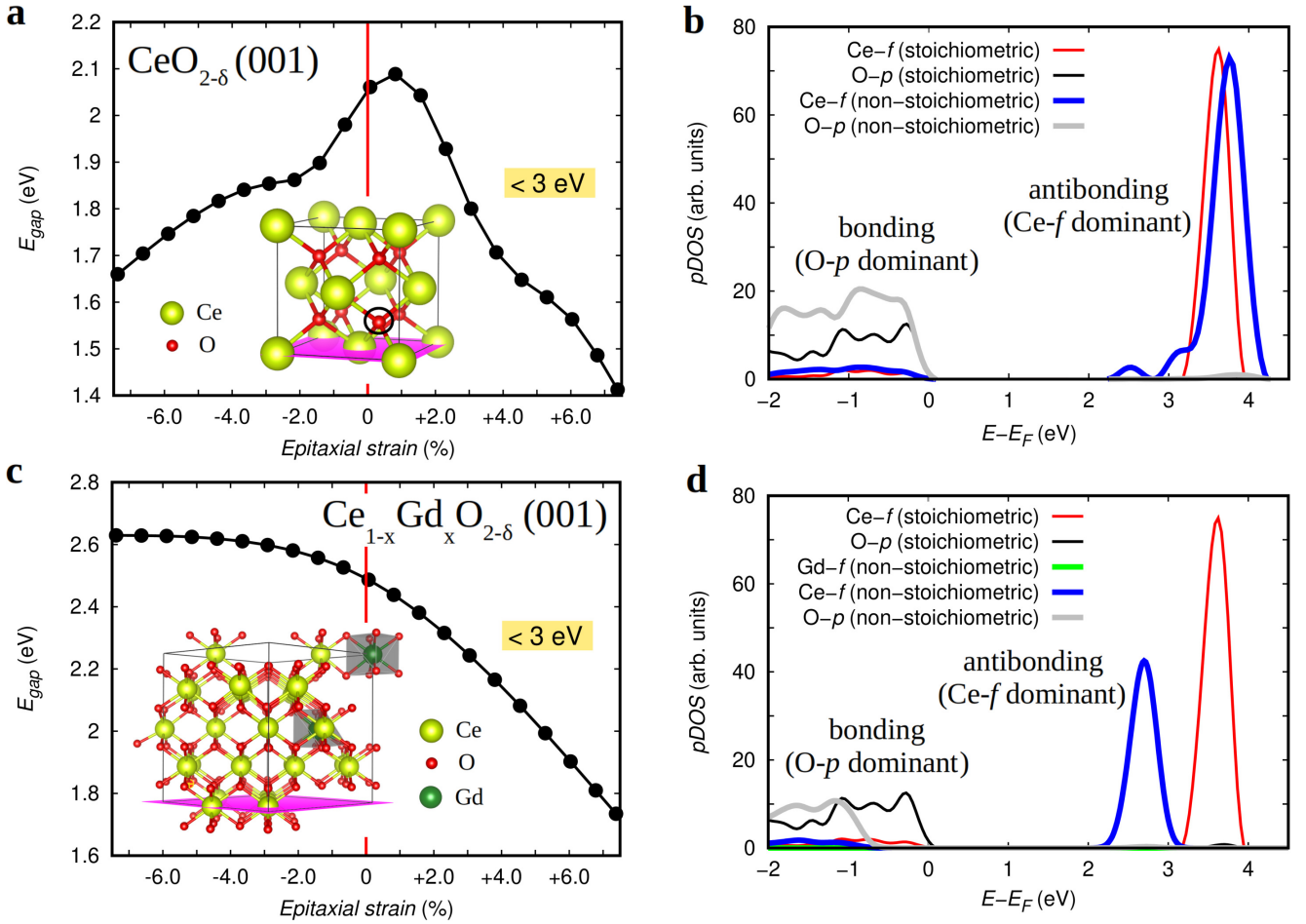


FIG. 3. Strain engineering of fluorite $\text{CeO}_{2-\delta}$ and $\text{Ce}_{1-x}\text{Gd}_x\text{O}_{2-\delta}$ (001). **a,c** Atomic structure and band gap of $\text{CeO}_{2-\delta}$ and $\text{Ce}_{1-x}\text{Gd}_x\text{O}_{2-\delta}$ (001), respectively, as a function of biaxial strain. The planes in which biaxial strain is applied are indicated in pink. The position of the oxygen vacancy created in $\text{CeO}_{2-\delta}$ (001) is indicated with a black circle. **b,d** Partial density of states calculated around the Fermi energy level in stoichiometric and non-stoichiometric $\text{CeO}_{2-\delta}$ and $\text{Ce}_{1-x}\text{Gd}_x\text{O}_{2-\delta}$ (001), respectively.

in $\text{Ce}_{1-2x}\text{Gd}_{2x}\text{O}_{2-x}$ (001) is very similar to that found in the undoped stoichiometric system (Fig.2c). The high delocalization of the Ce $4f$ orbitals forming the bottom of the CB in $\text{Ce}_{1-2x}\text{Gd}_{2x}\text{O}_{2-x}$ (001) (Fig.3d), however, leads to a noticeable reduction in the band gap as compared to undoped CeO_2 (001), which renders a practically constant E_g difference of ≈ 0.5 eV between the two systems across the entire range of η values.

C. Anatase TiO_2 (001)

Bulk TiO_2 is generally found in the rutile, anatase, or brookite phase. The rutile and anatase polymorphs find use in major industrial applications while brookite is of little technological relevance due to its difficult synthesis [43]. Rutile possesses tetragonal symmetry (space group $P4_2/mmm$) and a band gap of ≈ 3 eV, and is the energetically most favorable polymorph at room temperature.

Anatase also presents tetragonal symmetry (space group $I4_1/amd$) and its band gap is 3.2 eV [43]. Although the E_g of anatase is larger than that of rutile, the former phase typically exhibits superior photocatalytic activity owing to better positioning of the band edges and longer electron-hole recombination times [44, 45]. Hence it is of particular interest to investigate the influence of η on the band gap and band alignments of anatase, to see whether it is possible to further improve the photocatalytic performance of TiO_2 .

In anatase TiO_2 , each Ti ion is surrounded by six neighbouring oxygens and forms two characteristic bonds with them, Ti-O1 and Ti-O2, which are respectively two- and four-fold degenerate (Fig.4a). When biaxially strained in the (001) plane, the Ti-O1 bonds, which are oriented out-of-plane, become elongated under compressive strain and shortened under tensile strain (Fig.4b). Conversely, the Ti-O2 bonds, which are oriented at only a small angle to the (001) plane, are reduced under $\eta < 0$ and stretched under $\eta > 0$ (Fig.4b). Consequently, as in

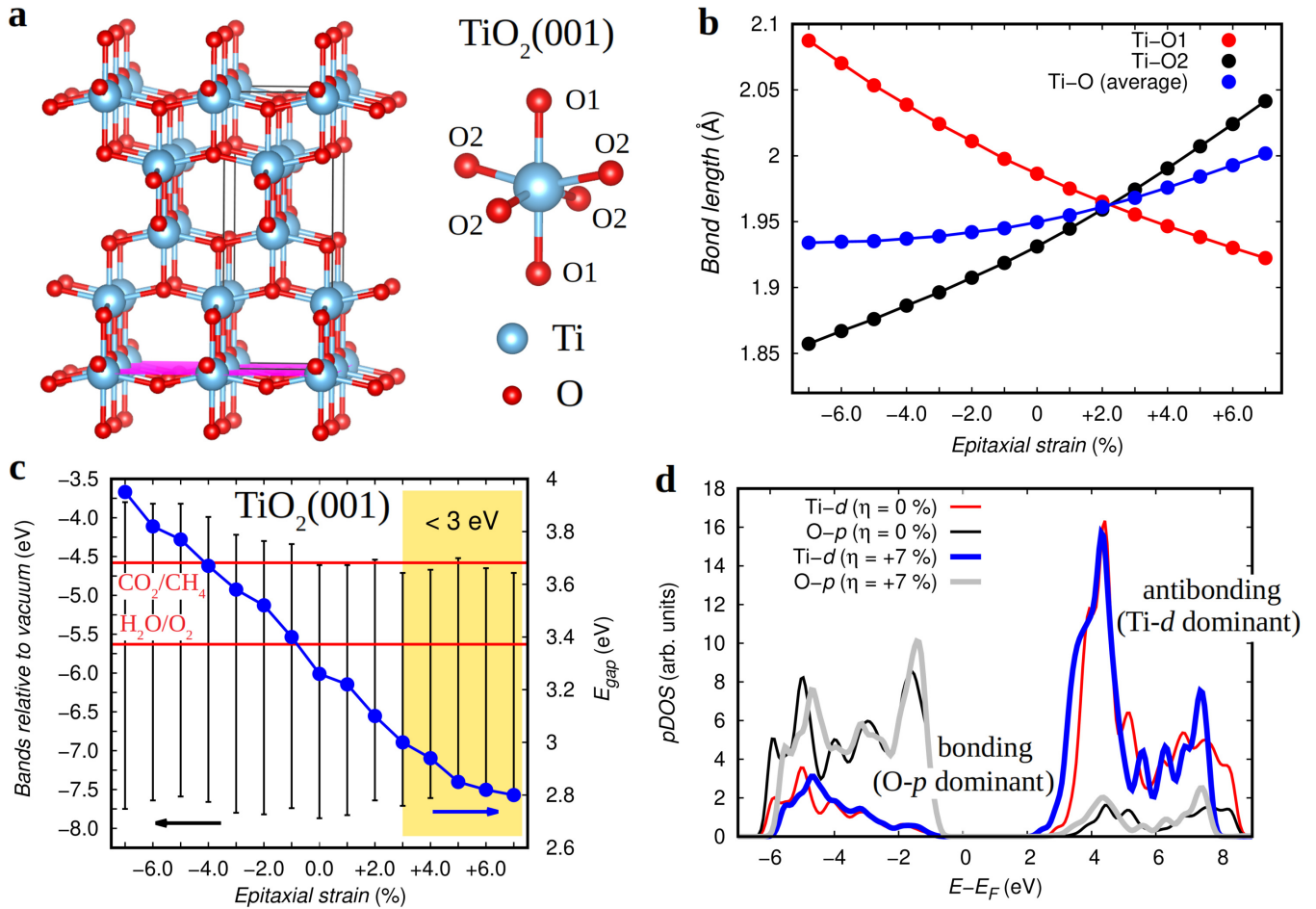


FIG. 4. Strain engineering of anatase $\text{TiO}_2(001)$. **a** Atomic structure of the analyzed thin film system. The plane in which biaxial strain is applied is indicated in pink. The local oxygen environment of the Ti atoms is shown. **b** Variation of different Ti-O bond lengths as a function of biaxial strain. **c** Band gap and band alignment changes induced by epitaxial strain. The region in which the system band gap is lower than 3 eV is highlighted in yellow. The redox potentials of interest are indicated with red horizontal lines. **d** Partial density of states calculated around the Fermi energy level at different η conditions.

most oxide semiconductors [31, 46], the average metal-oxygen bond length decreases under compressive strain (by 0.8% of the equilibrium value at $\eta = -7\%$) and increases under tensile strain (by 2.7% at $\eta = +7\%$).

Concerning the electronic properties, at zero biaxial strain we estimate $E_g = 3.3$ eV, which is in good agreement with the experimental value of 3.2 eV [43]. Under compressive strain, the band gap increases almost linearly, achieving a maximum value of 4.0 eV at $\eta = -7\%$ (Fig.4c). Under tensile strain, however, the band gap decreases steadily and becomes smaller than 3 eV at $\eta \approx +3\%$. A minimum band gap of 2.8 eV is estimated at the largest tensile distortion considered in this study (Fig.4c). We note that E_g remains indirect regardless of η (Supplementary Figure 5).

Such a regular E_g variation driven by biaxial strain across the entire range of strain values is in contrast to what was found for both the (111) and (001) orientations of CeO_2 , and can be explained in terms of the concurrent VB and CB edge shifts (Fig.4c). In bulk anatase,

the top of the VB is principally composed of oxygen 2p orbitals that form a bonding state with Ti 3d orbitals while the bottom of the CB is mostly composed of Ti 3d orbitals that form an antibonding state with O 2p orbitals (Fig.4d). Compressive strain has little effect on the position of the VB edge, due to a compensation effect between enhancement of bonding interactions (which tends to lower the VB) and increase in kinetic energy (which tends to increase the VB), whereas tensile strain tends to bring it higher in energy, owing to frustration of the bonding state (which dominates over the decrease in kinetic energy). Meanwhile, the position of the CB edge moves significantly higher in energy under compressive strain, due to a dominant increase in the kinetic energy (since the localization of the unoccupied Ti 3d orbitals appears to decrease slightly at $\eta < 0$, Supplementary Figure 6). Under tensile strain, the CB edge remains more or less constant owing to a small increase in the localization of the unoccupied Ti 3d orbitals at $\eta > 0$ (Fig.4d) that is counterbalanced by a decrease in the ki-

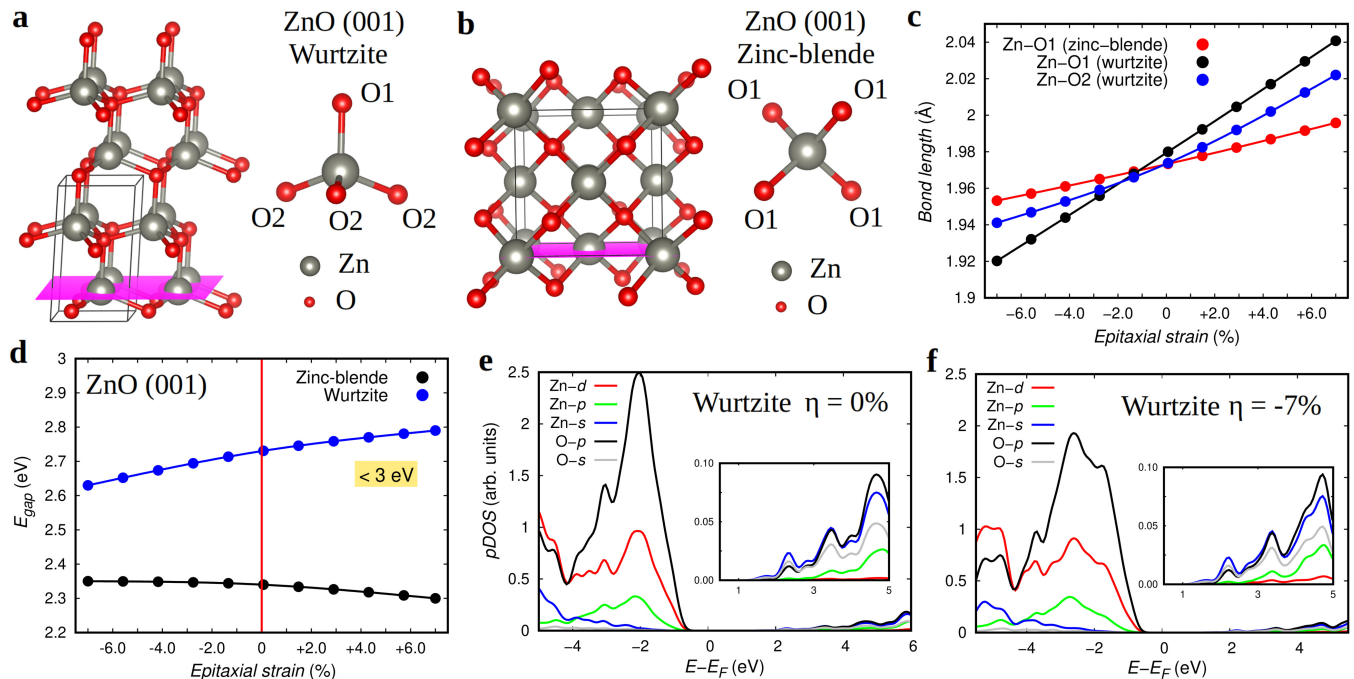


FIG. 5. Strain engineering of wurtzite and zinc-blende ZnO (001). Atomic structure of the analyzed **a** wurtzite thin film and **b** zinc-blende thin film. The planes in which biaxial strain is applied are indicated in pink. The local oxygen environment of the Zn atoms are shown. **c** Variation of different Zn-O bond lengths as a function of biaxial strain for the two crystal structures. **d** Band gap changes induced by epitaxial strain. **e** Partial density of states calculated around the Fermi energy level at equilibrium and **f** the maximum compressive biaxial stress considered in this study. The insets show the states at the conduction band minima in more detail.

netic energy. We note that, in analogy to CeO₂ thin films, the E_g shifts induced by η do not appear to be directly or exclusively correlated with the accompanying structural changes (i.e., the band gap variation is almost linear across the entire range of η values, Fig.4c, whereas the structural fluctuations are most prominent under tensile strain, Fig.4b).

The band alignments in anatase TiO₂ (001) are greatly affected by biaxial strain (Fig.4c). In the absence of planar stress, our calculations render a VB edge at -7.9 eV and CB at -4.6 eV relative to the vacuum level, which are in reasonable agreement with the available experimental data ($E_{\text{VB}}^{\text{expt}} = -7.6$ eV and $E_{\text{CB}}^{\text{expt}} = -4.4$ eV [44]). Under tensile strains of $> +3\%$, the band gap becomes smaller than 3 eV, the corresponding VB edge gets closer to the H₂O oxidation potential (for instance, at $\eta = +4\%$, E_{VB} is -7.6 eV), and the CB edge remains more or less constant around the value -4.6 eV. At these biaxial strain conditions, the energy of the CB edge is around the reduction potential of CO₂ (Fig.4c), hence tensilely strained anatase is predicted to be a suitable photocatalyst for driving the conversion of carbon dioxide into methane (CH₄) in aqueous environment under visible light [2]. Given the proximity of the CO₂ and water reduction potentials, it is likely that biaxially strained anatase TiO₂ ($\eta > 0$) is also a suitable material for driving the production of hydrogen fuel from H₂O under visible light.

D. Zinc-blende and wurtzite ZnO (001)

ZnO thin films are used in a wide variety of optoelectronic applications due to the relative abundance of their elements and direct band gap of ≈ 3.3 eV [47]. The two common ZnO polymorphs are wurtzite (hexagonal symmetry, space group $P6_3mc$) and zinc-blende (cubic symmetry, space group $F\bar{4}3m$), which are shown in Figs.5a-b. In wurtzite ZnO, each metal ion is coordinated to four neighboring oxygens and forms two characteristic metal-oxygen bond lengths, Zn-O1 and Zn-O2 (Fig.5a), which are single and three-fold degenerate, respectively. The evolution of the Zn-O1 and Zn-O2 distances as induced by η in the (001) plane are shown in Fig.5c. The Zn-O1 bond length is oriented out-of-plane and displays an anomalous behavior in the sense that it contracts under compressive biaxial strain and expands under tensile biaxial strain. Such an anomalous behavior, which is not observed in the Zn-O2 case (Fig.5c), probably is related to the negative thermal expansion observed in bulk ZnO [48]. On average, however, the mechanical behavior of wurtzite ZnO thin films is normal, namely, volume contraction at $\eta < 0$ and volume expansion at $\eta > 0$ relative to the unstrained reference system. Meanwhile, the zinc-blende structure, in which there is only one type of bond length, Zn-O1 (Fig.5b), presents a quite typical deformation behavior when biaxially strained in the (001) plane.

Figure 5d shows the band gaps of (001)-oriented ZnO thin films as a function of biaxial strain for the two crystal structures. In the absence of any strain, we estimate an E_g of 2.7 eV for the wurtzite phase and 2.4 eV for the zinc-blende phase. These results, in contrast to the systems analyzed previously, are not in good agreement with the experimental value of 3.3 eV [16]. A possible explanation for such a large band gap discrepancy may be the very low density of electronic states found at the bottom of the CB (Fig.5e), which may complicate the estimation of E_g both at the experimental and theoretical levels.

We find that the impact of η on the band gap of ZnO thin films is practically negligible (at least in comparison to the CeO₂ and TiO₂ cases), which is consistent with previous experimental observations [16]. For instance, according to our first-principles calculations, E_g for the wurtzite phase increases by just 2% at $\eta = +5\%$ and decreases by 3% at $\eta = -5\%$; in comparison, a reduction of 4% was obtained at $\eta \approx -5\%$ in experimental work [16]. Meanwhile, the band gap for the zinc-blende phase is changed by even smaller amounts, with only a 0.5% reduction at $\eta = +7\%$ and a 0.5% increase at $\eta = -7\%$ (note the opposite sign in the strain-driven E_g change as compared to the wurtzite case, Fig.5d). We note that the band gap of ZnO remains direct for all η (Supplementary Figure 7).

The reason behind the marginal effects of biaxial strain on the E_g of ZnO thin films seems to be related to the fact that the majority of electronic states forming both the top of the VB and the bottom of the CB are oxygen 2p orbitals (Figs.5e-f and Supplementary Figure 8). As a consequence of such an electronic band-structure symmetry the VB and CB edges are shifted very similarly when the crystal is subjected to external stress, thus leaving E_g practically invariant.

E. Explanation of the observed E_g trends using a simple model

In previous sections we have demonstrated by means of computational first-principles methods that biaxial strain can be used to alter substantially the optoelectronic and photocatalytic properties of some binary oxide semiconductors. However, the influence of η on the electronic band structure properties of binary oxide materials appears to be non-systematic and consequently difficult to predict. For instance, compressive biaxial strain hardly has any effect on the band gap of (001) CeO₂ thin films whereas it induces a large E_g increase in both (111) CeO₂ and (001) TiO₂ (Secs.III A–III C). On the other hand, the effects of η on the structural properties of binary oxides (provided that are stable and do not undergo phase transitions) are quite regular and relatively easy to foresee. Essentially, the metal-oxygen bond lengths for all the analyzed oxides are stretched by an average value of $\sim 1\%$ under moderate tensile biaxial strains and reduced

by roughly the same amount under compressive biaxial strains. These outcomes suggest that the origins of the optoelectronic and photocatalytic variations induced by biaxial strain cannot be explained uniquely in terms of simple structural changes [17, 19, 21]. In fact, a more sophisticated and general understanding of how photocatalytic activity can be tuned through η is highly desirable for improving the design and computational screening of potential energy materials.

According to well-established theories [49], the band gap of a material is influenced by the first Fourier coefficient of the crystal field, which results from the superposition of atomic potentials within the solid. The crystal field essentially depends on the interatomic distances, dielectric screening (or, alternatively, quantity of charge in the atomic environment), and density of atoms in the solid [50]. By shortening the atomic distances and/or weakening the dielectric screening, the crystal field is enhanced and as a result the band gap is widened. Conversely, by increasing the bond lengths and/or enhancing the dielectric screening the crystal field is depleted and the band gap is reduced. Therefore, there are two possible ways of modifying the crystal field along with the band gap in a structurally stable solid – changing its lattice parameters and/or its dielectric properties [50].

By combining deformation potential theory ($E_g(\sigma) \propto \sigma$, where σ represents mechanical stress) [17, 40] and the Kramers-Kronig relation ($E_g(\chi) \propto \chi^{-1/2}$, where χ represents the dielectric susceptibility of the material) [50, 51], we have deduced a simple analytical model that is able to describe qualitatively the band gap variations induced by biaxial strain on binary oxide semiconductors. Specifically, we express the η -driven relative variations of the band gap as:

$$\frac{\Delta E_g(\eta)}{E_g(0)} = -\frac{1}{2} \left(\frac{\Delta\chi(\eta)}{\chi(0)} + 2 \cdot \frac{\Delta d(\eta)}{d(0)} \right), \quad (1)$$

where the dependence of each term on biaxial strain is explicitly noted (for instance, “(0)” denotes unstrained), $\Delta A(\eta) \equiv A(\eta) - A(0)$, d represents the average metal-oxygen bond length, and the stress-strain relationship $\Delta\sigma/\sigma \approx -\Delta d/d$ has been used (the minus sign accounts for the fact that negative biaxial strains correspond to positive stresses and *vice versa*). Our model treats the effects of structural and dielectric fluctuations on the band gap as independent quantities, that is, $E_g(\sigma, \chi) = f(\sigma) \cdot g(\chi)$ where f and g are the two functions specified above; because of this, the model cannot be quantitatively exact. Nevertheless, in spite of its limitations, this model provides a general and physically intuitive understanding of the results reported in the previous sections for binary oxides without the need to consider the details of the specific band structure of each material.

Table I shows the $\Delta E_g/E_g$ values obtained for biaxially strained CeO₂, TiO₂, and ZnO thin films at the largest η 's considered in this study using both DFT methods (exact) and the analytical model expressed in Eq.(1) (approximate). The corresponding $\Delta\chi/\chi$ and $\Delta d/d$ values

	$\frac{\Delta\chi}{\chi}$		$\frac{\Delta d}{d}$		$\frac{\Delta E_g}{E_g}$ (%) [model]		$\frac{\Delta E_g}{E_g}$ (%) [DFT]		
	η	-7%	+7%	-7%	+7%	-7%	+7%	-7%	+7%
CeO ₂ (111)		-0.063	-0.043	-0.014	0.025	+5	-1	+10	-4
CeO ₂ (001)		0.033	0.136	-0.029	0.038	+1	-11	+2	-29
(a) TiO ₂ (001)		-0.109	0.063	-0.008	0.027	+6	-6	+21	-14
(w) ZnO (001)		0.022	-0.039	-0.020	0.026	+1	-1	-4	+2
(zb) ZnO (001)		0.074	0.061	-0.010	0.012	-3	-4	+1	-1

TABLE I. Relative band gap changes calculated at the maximum compressive and tensile biaxial stresses considered in this study for different semiconductor binary oxides. $\Delta\chi$ and Δd stand for the variation in the dielectric susceptibility and average metal-oxygen bond length as referred to the unstrained case. (a), (w), and (zb) stand for anatase, wurtzite, and zinc-blende structures, respectively. [model] refers to the relative band gap variations estimated with the analytical model expressed in Eq.(1), while [DFT] to those values obtained directly from the DFT calculations.

are also reported in Table I. The dielectric susceptibility is calculated with the formula $\chi = \epsilon_\infty - 1$, where ϵ_∞ represents the ion-clamped dielectric constant of the material (estimated with perturbation DFT techniques) [30]. In the case of CeO₂ and TiO₂ thin films Eq.(1) reproduces the relative band gap variations induced by biaxial strain correctly (albeit only at the qualitative level). For example, the analytical model predicts a reduction (increase) in E_g under tensile (compressive) strain and the largest band gap variation is found for (001)-oriented CeO₂ thin films at $\eta > 0$. On the other hand, the $\Delta E_g/E_g$ values estimated with Eq.(1) are systematically lower in magnitude than those calculated directly with DFT techniques by roughly a factor of 2. In the case of ZnO thin films, the analytical model consistently predicts band gap variations similar in magnitude to those obtained with DFT methods; however, the corresponding signs are reversed in most cases. This comparison indicates that the limitations of Eq.(1) become more pronounced when trying to reproduce small $\Delta E_g/E_g$ values (as expected, given the qualitative nature of the model).

The data shown in Table I along with the analytical model in Eq.(1) allow us to understand better the origins of the non-systematic E_g trends found in binary oxides under biaxial strain. As mentioned earlier, the $\Delta d/d$ changes induced by η are systematic and general to most materials, but the $\Delta\chi/\chi$ variations are not. For example, for (001)-oriented CeO₂ thin films, the dielectric susceptibility always increases with increasing magnitude of biaxial strain, irrespective of whether it is tensile or compressive. In contrast, for (001)-oriented TiO₂ anatase thin films, compressive (tensile) strain produces a reduction (increase) in χ . Consequently, according to Eq.(1) and the data in Table I, the changes induced by

η on the dielectric properties of each material are ultimately responsible for the irregular behavior observed in $\Delta E_g/E_g$. For instance, the large band gap changes found for (001)-oriented CeO₂ thin films under $\eta > 0$ and for (001)-oriented TiO₂ anatase thin films under $\eta < 0$ can be traced to the $\Delta\chi/\chi$ and $\Delta d/d$ terms having the same sign and hence being additive (Table I). Likewise, the small band gap changes found for (111)-oriented CeO₂ thin films under $\eta > 0$ and for wurtzite (001)-oriented ZnO thin films either under $\eta > 0$ or $\eta < 0$ can be traced to the $\Delta\chi/\chi$ and $\Delta d/d$ terms having opposite signs (Table I). The new insights presented in this section in terms of the role of dielectric susceptibility changes can be useful for better understanding the electronic behavior of binary oxide semiconductors subjected to biaxial strain, and for improving the design of potential photocatalytic materials.

IV. CONCLUSIONS

In this study we have demonstrated by means of first-principles methods that biaxial strain can be used to tune the optoelectronic and photocatalytic properties of binary oxide semiconductors in a substantial and predictable manner. The changes caused by η on the band gap of simple oxides can be understood in terms of structural and dielectric susceptibility variations that alter the crystal field and thus the bonding-antibonding splitting. The structural changes induced by biaxial strain on binary oxides are quite general and regular, but the accompanying changes in electronic screening are not systematic. As a result of those two distinct and sometimes opposing contributions, we find that the biaxial

strain has different effects on the band gap of different oxides – the band gaps of stoichiometric CeO₂ and anatase TiO₂ can be reduced below 3 eV under moderate tensile strains of $\approx +2\%$ and $+3\%$, respectively, whereas the band gap of ZnO is only marginally affected (namely, $|\Delta E_g|/E_g \sim 1\%$) by $|\eta|$'s as large as 7%. We have also shown that η has a significant influence on the band gap of non-stoichiometric and metal-doped binary oxide semiconductors. Furthermore, biaxial strain can alter significantly the energy levels of the valence and conduction band edges. In particular, we find that under tensile strain (111)–oriented CeO₂ and (001)–oriented TiO₂ thin films become suitable photocatalysts for driving the splitting of H₂O into H₂ and O₂ and the reduction of CO₂ into CH₄, respectively, in aqueous environment under sun-

light. Strain engineering, therefore, offers a systematic design tool for achieving improved photocatalytic activity in binary oxide semiconductors, either on its own or in combination with other nanostructuring approaches.

ACKNOWLEDGMENTS

Computational resources and technical assistance were provided by the Australian Government and the Government of Western Australia through the National Computational Infrastructure (NCI) and Magnus under the National Computational Merit Allocation Scheme and The Pawsey Supercomputing Centre.

-
- [1] Fajrina, N. & Tahir, M. A critical review in strategies to improve photocatalytic water splitting towards hydrogen production. *Int. J. Hydrog. Energy* **44**, 540 (2019).
- [2] Xie, S., Zhang, Q., Liu, G. & Wang, Y. Photocatalytic and photoelectrocatalytic reduction of CO₂ using heterogeneous catalysts with controlled nanostructures. *Chem. Commun.* **52**, 35 (2016).
- [3] Shenoy, J., Hart, J. N., Grau-Crespo, R., Allan, N. L. & Cazorla, C. Mixing Thermodynamics and Photocatalytic Properties of GaP-ZnS solid solutions. *Adv. Theory Simul.* **2**, 1800146 (2019).
- [4] Park, H., Kim, H.-I., Moon, G.-H. & Wonyong, C. Photoinduced charge transfer processes in solar photocatalysis based on modified TiO₂. *Energy Environ. Sci.* **9**, 411 (2016).
- [5] Rahimi, N., Pax, R. A. & Gray, E. M. Review of functional titanium oxides. I: TiO₂ and its modifications. *Prog. Solid State Ch.* **44**, 86 (2016).
- [6] Castano, C. E., O'Keefe, M. J. & Farenholtz, W. G. Cerium-based oxide coatings. *Curr. Opin. Solid St. M.* **19**, 69 (2015).
- [7] Montini, T., Melchionna, M., Monai, M. & Fornasiero, P. Fundamentals and catalytic applications of CeO₂-based materials. *Chem. Rev.* **116**, 5987 (2016).
- [8] Kowalska, E., Remita, H., Colbeau-Justin, C., Hupka, J. & Belloni, J. Modification of titanium dioxide with platinum ions and clusters: Application in photocatalysis. *J. Phys. Chem. C* **112**, 1124 (2008).
- [9] Asahi, R., Morikawa, T., Ohwaki, T., Aoki, K. & Taga, Y. Visible-light photocatalysis in nitrogen-doped titanium oxides. *Science* **293**, 269 (2001).
- [10] Mitsudome, T., Mikami, Y., Matoba, M., Mizugaki, T., Jitsukawa, K. & Kaneda, K. Design of a silver-cerium dioxide core-shell nanocomposite catalyst for chemoselective reduction reactions. *Angew Chem. Int. Ed.* **51**, 136 (2012).
- [11] Takanabe, K. Photocatalytic water splitting: Quantitative approaches toward photocatalyst by design. *ACS Catal.* **7**, 8006 (2017).
- [12] Hu, S., Cazorla, C., Xiang, F., Ma, H., Wang, J., Wang, J., Wang, X., Ulrich, C., Chen, L. & Seidel, J. Strain control of giant magnetic anisotropy in metallic perovskite SrCoO_{3- δ} thin films. *ACS Appl. Mater. Interfaces* **10**, 22348 (2018).
- [13] Heo, Y., Hu, S., Sharma, P., Kim, K.-E., Jang, B.-K., Cazorla, C., Yang, C.-H., & Seidel, J. Impact of isovalent and aliovalent doping on mechanical properties of mixed phase BiFeO₃. *ACS Nano* **11**, 2805 (2017).
- [14] Gopal, C. B. *et al.* Equilibrium oxygen storage capacity of ultrathin CeO_{2- δ} depends non-monotonically on large biaxial strain. *Nat. Commun.* **8**, 15360 (2017).
- [15] Benson, E. E. *et al.* Semiconductor-to-metal transition in rutile TiO₂ induced by tensile strain. *Chem. Mater.* **29**, 2173 (2017).
- [16] Choi, H.-J., Jang, W., Mohanty, B. C., Jung, Y.S., Soon, A. & Cho, Y.-S. Origin of prestress-driven optical modulations of flexible ZnO thin films processed in stretching mode. *J. Phys. Chem. Lett.* **9**, 5934 (2018).
- [17] Yin, W.-J., Che, S., Yang, J.-H., Gong, X.-G., Yan, Y. & Wei, S.-H. Effective band gap narrowing of anatase TiO₂ by strain along a soft crystal direction. *Appl. Phys. Lett.* **96**, 221901 (2010).
- [18] Kelaidis, N., Kordatos, A., Christopoulos, S.-R.G. & Chroneos, A. A roadmap of strain in doped anatase TiO₂. *Sci. Rep.* **8**, 12790 (2018).
- [19] Zhou, W., Liu, Y., Yang, Y. & Wu, P. Band gap engineering of SnO₂ by epitaxial strain: Experimental and theoretical investigations. *J. Phys. Chem. C* **118**, 6448 (2014).
- [20] Yan, Q. M., Rinke, P., Winkelnkemper, M., Qteish, A., Bimberg, D., Scheffler, M. & Van de Walle, C. G. Strain effects and band parameters in MgO, ZnO, and CdO. *Appl. Phys. Lett.* **101**, 152105 (2012).
- [21] Wagner, J.-M. & Bechstedt, F. Properties of strained wurtzite GaN and AlN: Ab initio studies. *Phys. Rev. B* **66**, 115202 (2002).
- [22] Cazorla, C. The role of density functional theory methods in the prediction of nanostructured gas-adsorbent materials. *Coord. Chem. Rev.* **300**, 142 (2015).
- [23] Cazorla, C., Rojas-Cervellera, V. & Rovira, C. Calcium-based functionalization of carbon nanostructures for peptide immobilization in aqueous media. *J. Mater. Chem.* **22**, 19684 (2012).
- [24] Cazorla, C. & Boronat, B. Simulation and understanding of atomic and molecular quantum crystals. *Rev. Mod. Phys.* **89**, 035003 (2017).

- [25] Perdew, J. P., Ruzsinszky, A., Csonka, G. I., Vydrov, O. A., Scuseria, G. E., Constantin, L. A., Zhou, X. & Burke, K. Restoring the density-gradient expansion for exchange in solids and surfaces. *Phys. Rev. Lett.* **100**, 136406 (2008).
- [26] Kresse, G. & Fürthmüller, J. Efficient iterative schemes for ab initio total-energy calculations using a plane-wave basis set. *Phys. Rev. B* **54**, 11169 (1996); Kresse, G. & Joubert, D. From ultrasoft pseudopotentials to the projector augmented-wave method. *Phys. Rev. B* **59**, 1758 (1999).
- [27] Dudarev, S. L., Botton, G. A., Savrasov, S. Y., Humphreys, C. J. & Sutton, A. P. Electron-energy-loss spectra and the structural stability of nickel oxide: An LSDA+U study. *Phys. Rev. B* **57**, 1505 (1998).
- [28] Blöchl P. E. Projector augmented-wave method. *Phys. Rev. B* **50**, 17953 (1994).
- [29] Monkhorst, H. J. & Pack, J. D. Special points for Brillouin-zone integrations. *Phys. Rev. B* **13**, 5188 (1976).
- [30] Cazorla, C. & Stengel, M. Electrostatic engineering of strained ferroelectric perovskites from first-principles. *Phys. Rev. B* **92**, 214108 (2015).
- [31] Cazorla, C. Lattice effects on the formation of oxygen vacancies in perovskite thin films. *Phys. Rev. Appl.* **7**, 044025 (2017).
- [32] Cazorla, C., Diéguez, O. & Íñiguez, J. Multiple structural transitions driven by spin-phonon couplings in a perovskite oxide. *Sci. Adv.* **3**, e1700288 (2017).
- [33] Cazorla, C. & Íñiguez J. Giant direct and inverse electrocaloric effects in multiferroic thin films. *Phys. Rev. B* **98**, 174105 (2018).
- [34] Krukau, A. V., Vydrov, O. A., Izmaylov, A. F. & Scuseria, G. E. Influence of the exchange screening parameter on the performance of screened hybrid functionals. *J. Chem. Phys.* **125**, 224106 (2006).
- [35] Moses, P. G., Miao, M., Yan, Q., & Van de Walle, C. G. Hybrid functional investigations of band gaps and band alignments for AlN, GaN, InN, and InGaN. *J. Chem. Phys.* **134**, 084703 (2011).
- [36] Baldereschi, A., Baroni, S. & Resta, R. Band offsets in lattice-matched heterojunctions: A model and first-principles calculations for GaAs/AlAs. *Phys. Rev. Lett.* **61**, 734 (1988).
- [37] Cazorla, C. & Stengel, M. First-principles modeling of Pt/LaAlO₃/SrTiO₃ capacitors under an external bias potential. *Phys. Rev. B* **85**, 075426 (2012).
- [38] Goubin, F., Rocquefelte, X., Whangbo, M.-H., Montardi, Y., Brec, R. & Jobic, S. Experimental and theoretical characterization of the optical properties of CeO₂, SrCeO₃, and Sr₂CeO₄ containing Ce⁴⁺ (*f*⁰) ions. *Chem. Mater.* **16**, 662 (2004).
- [39] Wen, X.-J., Niu, C.-G., Zhang, L., Liang, C. & Zeng, G.-M. A novel Ag₂O/CeO₂ heterojunction photocatalysts for photocatalytic degradation of enrofloxacin: possible degradation pathways, mineralization activity and an in depth mechanism insight. *Appl. Catal. B-Environ.* **221**, 701 (2018).
- [40] Wei, S.-H. & Zunger, A. Predicted band-gap pressure coefficients of all diamond and zinc-blende semiconductors: Chemical trends. *Phys. Rev. B* **60**, 5404 (1999).
- [41] Mofarah, S. S., Adabifiroozjahi, E., Webster, R., Koshy, P., Nekouei, R. K., Lim, S., Yao, Y., Cazorla, C., Liu, Z., Lambropoulos, N. & Sorrell, C. C. Proton-assisted creation of controllable volumetric oxygen vacancy in ultrathin ceria for pseudo-capacitive energy storage applications. *Nat. Commun.* **10**, 2594 (2019).
- [42] Korobko, R., Patlolla, A., Kossov, A., Wachtel, E., Tuller, H. L., Frenkel, A. I. & Lubomirsky, I. Giant electrostriction in Gd-Doped ceria. *Adv. Mater.* **24**, 5857 (2012).
- [43] Yamada, Y. & Kanemitsu, Y. Determination of electron and hole lifetimes of rutile and anatase TiO₂ single crystals. *Appl. Phys. Lett.* **101**, 133907 (2012).
- [44] Bätzill, M. Fundamental aspects of surface engineering of transition metal oxide photocatalysts. *Energy Environ. Sci.* **4**, 3275 (2011).
- [45] Choi, W., Termin, A. & Hoffmann, M. R. The role of metal ion dopants in quantum-sized TiO₂: Correlation between photoreactivity and charge carrier recombination dynamics. *J. Phys. Chem. C* **98**, 13669 (1994).
- [46] Bousquet, E., Spaldin, N. A. & Ghosez, P. Strain-induced ferroelectricity in simple rocksalt binary oxides. *Phys. Rev. Lett.* **104**, 037601 (2010).
- [47] Ozgur, U., Alivov, Y. I., Liu, C., Teke, A., Reshchikov, M. A., Dogan, S., Avrutin, V., Cho, S.-J. & Morkoc, H. A comprehensive review of ZnO materials and devices. *J. Appl. Phys.* **98**, 041301 (2005).
- [48] Wang, Z., Wang, F., Wang, L., Jia, Y. & Sun, Q. First-principles study of negative thermal expansion in zinc oxide. *J. Appl. Phys.* **114**, 063508 (2013).
- [49] Omar, M. A. *Elementary Solid State Physics: Principles and Applications* (New York: Addison-Wesley, 1975).
- [50] Sun, C. Q., Sun, X. W., Tay, B. K., Lau, S. P., Huang, H. T. & Li, S. Dielectric suppression and its effect on photoabsorption of nanometric semiconductors. *J. Phys. D: Appl. Phys.* **34**, 2359 (2001).
- [51] Haiming, L. & Meng, X. Correlation between band gap, dielectric constant, Young's modulus and melting temperature of GaN nanocrystals and their size and shape dependences. *Sci. Rep.* **5**, 16939 (2015).